PCCP

ROYAL SOCIETY OF CHEMISTRY

PAPER

View Article Online
View Journal | View Issue

Check for updates

Cite this: *Phys. Chem. Chem. Phys.*, 2023, **25**, 13933

Conformational and state-specific effects in reactions of 2,3-dibromobutadiene with Coulomb-crystallized calcium ions†‡

Ardita Kilaj,§[a] Silvan Käser,¶[a] Jia Wang,¶‖[b] Patrik Straňák,¶**[a] Max Schwilk,[a] Lei Xu,[a] O. Anatole von Lilienfeld,[acdef] Jochen Küpper,*[bghi] Markus Meuwly*[aj] and Stefan Willitsch*[a]

Received 28th March 2023,
Accepted 27th April 2023

DOI: 10.1039/d3cp01416a

rsc.li/pccp

Recent advances in experimental methodology enabled studies of the quantum-state- and conformational dependence of chemical reactions under precisely controlled conditions in the gas phase. Here, we generated samples of selected *gauche* and *s-trans* 2,3-dibromobutadiene (DBB) by electrostatic deflection in a molecular beam and studied their reaction with Coulomb crystals of laser-cooled Ca^+ ions in an ion trap. The rate coefficients for the total reaction were found to strongly depend on both the conformation of DBB and the electronic state of Ca^+. In the $(4p)^2P_{1/2}$ and $(3d)^2D_{3/2}$ excited states of Ca^+, the reaction is capture-limited and faster for the *gauche* conformer due to long-range ion–dipole interactions. In the $(4s)^2S_{1/2}$ ground state of Ca^+, the reaction rate for *s-trans* DBB still conforms with the capture limit, while that for *gauche* DBB is strongly suppressed. The experimental observations were analysed with the help of adiabatic capture theory, *ab initio* calculations and reactive molecular dynamics simulations on a machine-learned full-dimensional potential energy surface of the system. The theory yields near-quantitative agreement for *s-trans*-DBB, but overestimates the reactivity of the *gauche*-conformer compared to the experiment. The present study points to the important role of molecular geometry even in strongly reactive exothermic systems and illustrates striking differences in the reactivity of individual conformers in gas-phase ion–molecule reactions.

Introduction

Gas-phase ion–molecule reactions play a key role in the ionosphere of the earth and in interstellar clouds[1–3] as well as in the context of catalysis, where gas-phase studies can help to elucidate the mechanisms of bond activation.[4,5] As experiments are advancing to probe ever more complex systems,[6,7] the precise molecular geometry, and in particular the molecular conformation, becomes increasingly important for the reaction dynamics. Thus, new experimental methods become necessary which are capable of isolating individual conformers in the gas phase in order to study their specific reactivities. In this context, we recently developed a new technique for the investigation of conformational effects in ion–molecule reactions based on trapped and laser-cooled atomic ions forming Coulomb crystals.[6,8] Coulomb crystals can be considered as reaction vessels in which reactant and product molecular ions can be co-trapped and cooled sympathetically by the laser-cooled species.[9,10] The neutral co-reactant is introduced into the experiment in a molecular beam passing through an inhomogeneous electrostatic field where molecular conformations with different electric dipole moments in the laboratory

---

[a] Department of Chemistry, University of Basel, Klingelbergstrasse 80, 4056, Basel, Switzerland. E-mail: m.meuwly@unibas.ch, stefan.willitsch@unibas.ch
[b] Center for Free-Electron Laser Science CFEL, Deutsches Elektronen-Synchrotron DESY, Notkestr. 85, 22607 Hamburg, Germany. E-mail: jochen.kuepper@cfel.de
[c] Vector Institute for Artificial Intelligence, Toronto, ON, M5S 1M1, Canada
[d] Departments of Chemistry, Materials Science and Engineering, and Physics, University of Toronto, St. George Campus, Toronto, ON M5S 3H6, Canada
[e] Machine Learning Group, Technische Universität Berlin, 10587 Berlin, Germany
[f] Berlin Institute for the Foundations of Learning and Data - BIFOLD, Germany
[g] Department of Physics, Universität Hamburg, Luruper Chaussee 149, 22761 Hamburg, Germany
[h] Department of Chemistry, Universität Hamburg, Martin-Luther-King-Platz 6, 20146 Hamburg, Germany
[i] Center for Ultrafast Imaging, Universität Hamburg, Luruper Chaussee 149, 22761 Hamburg, Germany
[j] Department of Chemistry, Brown University, Providence, RI 02912, USA

† In memoriam Max Schwilk (1986–2022).

‡ Electronic supplementary information (ESI) available. See DOI: https://doi.org/10.1039/d3cp01416a

§ Present address: Novartis Institutes for Biomedical Research, Fabrikstrasse 2, 4056 Basel, Switzerland.

¶ These authors contributed equally to the present work.

‖ Present address: Department of Chemistry, University of Hawaii at Manoa, Honolulu, HI 96822, USA.

** Present address: Fraunhofer Institute for Applied Solid State Physics IAF, Tullastrasse 72, 79108 Freiburg, Germany.

frame are spatially separated.[11–17] This approach recently enabled studies of reactions of ions with individual conformations[14,18] and also selected rotational states[19] of neutral molecules, which pointed to the important role of conformer- and state-specific long-range interactions governing both the dynamics and kinetics in these systems. In these cases, capture theories[20–22] could be successfully applied to model rate coefficients. To gain deeper insight into fundamental mechanisms of conformational dynamics in gas-phase ion–molecule processes, we here performed kinetic measurements of trapped Ca^+ ions reacting with a molecular beam of 2,3-dibromobutadiene (DBB) molecules using an electrostatic deflector[13] to separate its *gauche* and *s-trans* conformers.[17] Already a number of previous studies focused on ion–molecule reactions of atomic ions with supersonic beams or thermal samples of neutral molecules, see, *e.g.*, ref. 4 and 5 for an overview. Studies on singly charged alkaline-earth ions, *e.g.*, Mg^+[23,24] and Ca^+,[14,25–29] often found that fast reactions proceeded from excited electronic states of the metal ion while reactions involving the ground state were found to be kinetically hindered. By contrast, we showed that for the present system the reaction rate of Ca^+ with *s-trans* DBB is capture-limited irrespective of the electronic state of Ca^+, *i.e.* $(4s)^2S_{1/2}$, $(4p)^2P_{1/2}$ or $(3d)^2D_{3/2}$. Conversely, for the *gauche* conformer we found that the reaction is capture-limited only with Ca^+ in its $^2P_{1/2}$ or $^2D_{3/2}$ excited states. In the $^2S_{1/2}$ ground state, however, the reaction rate is strongly suppressed pointing to a pronounced conformational effect governing the ground-state reaction dynamics.

To rationalize the experimental findings, we modelled the kinetics and dynamics using adiabatic capture theory[30] and reactive molecular dynamics simulations on a full-dimensional potential energy surface (PES) of the system trained on the results of *ab initio* calculations by a neural network (NN). The theory yields excellent agreement with experiment for the reaction of *s-trans*-DBB, but overestimates the reactivity of the *gauche*-conformer by almost an order of magnitude suggesting the presence of an as yet unaccounted dynamic bottleneck along the *gauche* reaction pathway. Possible explanations are discussed. The present study highlights the important role of molecular conformation in gas-phase ion–molecule reactions of polyatomic species and the role of both long-range and short-range effects in determining conformational differences in chemical reactivity.

Results

Experimental setup

The experimental setup, Fig. 1a, consisted of a molecular beam apparatus interfaced with an ion trap, see Methods and ref. 14, 17 and 19. Briefly, an internally cold beam of the neutral reaction partner DBB seeded in neon carrier gas was formed by pulsed supersonic expansion and passed through a series of skimmers and an electrostatic deflector before it reached the ion trap. The deflector's inhomogeneous electric field allowed the separation of the polar *gauche* conformer of DBB (dipole moment μ_{gauche} = 2.29 D) from the apolar *s-trans* conformer ($\mu_{s\text{-}trans}$ = 0). In the ion trap, laser-cooled Ca^+ ions formed a Coulomb crystal[6] and served as a collision target for the molecular beam. Different conformers of DBB were selectively brought into reaction with the Ca^+ ions by vertically tilting the molecular beam apparatus.

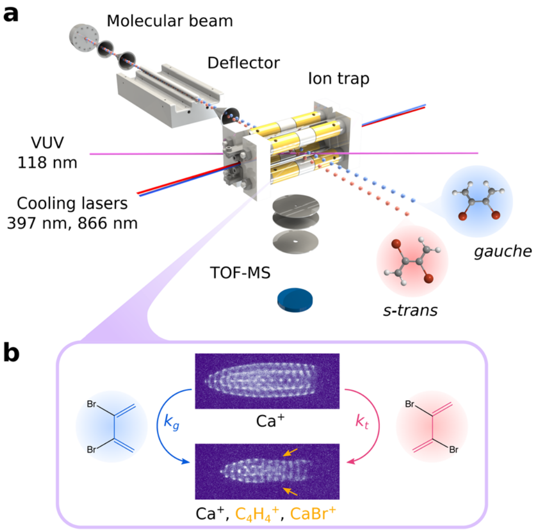

Fig. 1 Overview of the experiment. (a) Schematic of the experimental setup. The two conformers of DBB are separated by electrostatic deflection in a molecular beam and directed at an ion trap holding a Coulomb crystal of trapped Ca^+ ions. Reaction kinetics are measured by ion extraction into a TOF-MS. (b) Depiction of the reaction between the *gauche* and *s-trans* conformers of DBB with Ca^+, each featuring a different reaction rate coefficient k_g and k_t, respectively. Fluorescence images of the initial laser-cooled Ca^+ Coulomb crystal (top) and after reaction with DBB (bottom). Arrows indicate regions where ions heavier than Ca^+ accumulate in the trap.

The reaction of Ca^+ with the *gauche* and *s-trans* DBB conformers proceeded *via* individual pathways with bimolecular reaction rate coefficients k_g and k_t, respectively (Fig. 1b). Throughout the reaction, the fluorescence of Ca^+ ions due to laser cooling on the $^2S_{1/2} \rightarrow {}^2P_{1/2}$ transition at 397 nm was imaged onto a camera (Fig. 1b). As the reactions progressed, the Coulomb crystals changed shape due to loss of Ca^+ ions and accumulation of heavier product ions around the Ca^+ core. Quantitative analysis of the reaction kinetics and products was performed by ejecting the trapped ions into a time-of-flight mass-spectrometer (TOF-MS) radially coupled to the ion trap.[31]

Reaction products

As a first step, the product ions of the reaction were characterized using the TOF-MS after a reaction time of 2 minutes (Fig. 2). The electrostatic deflector was switched off and a high-flux molecular beam of DBB with a thermal (300 K) *gauche* : *trans* conformer mixture of 1 : 3.3[17] was directed at the ion trap. TOF-MS traces averaged over 45 experiments are displayed in Fig. 2a and compared against a control experiment in which the molecular beam did not contain DBB (grey inverted trace). Besides a dominant peak corresponding to Ca^+ (40 u) at a time of flight of t = 12.9 μs, the spectra contain four main features

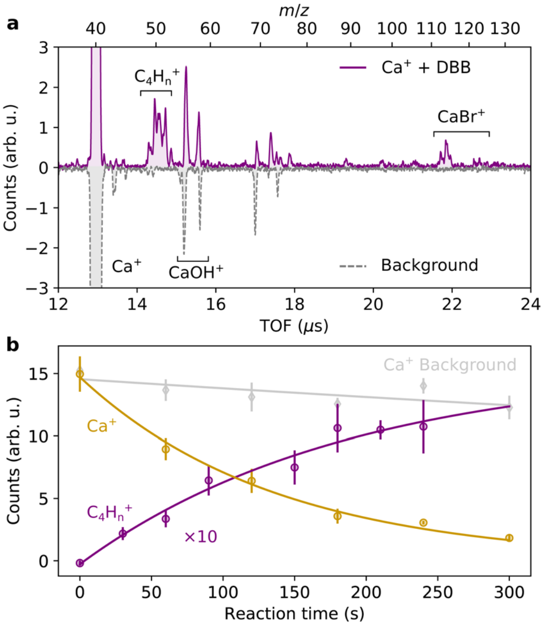

Fig. 2 Reaction products. (a) TOF mass spectrum of the trapped ions after reaction (purple) and comparison to a Coulomb crystal of Ca^+ exposed to a molecular beam without DBB (gray). Each trace is an average of at least 45 individual measurements. (b) Reaction-time-dependent ion counts measured using the TOF-MS: depletion of Ca^+ (yellow) with corresponding background measurement (grey) and formation of $C_4H_n^+$ (purple). The $C_4H_n^+$ signal is rescaled for clarity. Error bars represent standard errors of three independent measurements.

that were assigned to specific molecular compounds with assistance of molecular dynamics simulations (see ESI,‡ Section S1). The main background signal at $t \approx 15$ μs corresponds to $CaOH^+$ (57 u), formed by the reaction of Ca^+ with residual water in the vacuum chamber (pressure 4×10^{-10} mbar). Another weaker impurity signal around $t \approx 17$ μs with approximate mass 72 u could be due to CaO_2^+.[29] Clearly, ions forming uniquely as products of the reaction Ca^+ + DBB were observed at $t \approx 14.5$ μs and $t \approx 22$ μs and were identified as $C_4H_n^+$ ($n = 2$–4, 50–52 u) and $CaBr^+$ (119 and 121 u), respectively. Another possible reaction product could be $CaBr_2^+$ (200 u), which was however not detected (ESI,‡ Section S1). Excess kinetic energy after the reaction or excitation by the UV cooling laser for Ca^+ could lead to its rapid dissociation to $CaBr^+$. A (H)Br^+ fragment was also not detected. Consequently, the reaction leads to a Br-abstraction from DBB and a localisation of the charge on either $CaBr^+$ or the butadiene moiety. The observation of $C_4H_n^+$ fragments points to H-loss from the expected $C_4H_4^+$ product.[32] The reaction kinetics for the observed products $C_4H_n^+$ and $CaBr^+$ can thus be modeled using the following equations,

$$Ca^+ + C_4H_4Br_2 \xrightarrow{k^{(1)}} CaBr^+ + C_4H_4Br \tag{1}$$

$$\xrightarrow{k^{(2)}} C_4H_n^+ + CaBr_2 + (4-n)H \tag{2}$$

with bimolecular rate coefficients $k^{(1,2)}$. To explore the reaction kinetics, the number of Ca^+ and $C_4H_n^+$ ions in the Coulomb crystals were determined as a function of reaction time using the TOF-MS in high-resolution mode[31] in separate experiments (Fig. 2b). The event rate of $CaBr^+$ detection was too low to measure its kinetics of formation with sufficient statistics. Fig. 2b compares the decrease of Ca^+ ions in the crystal due to reaction with DBB (yellow data points) with the formation of the product fragment $C_4H_n^+$ (purple points). The data of the latter are scaled by a factor of 10 for clarity. For reference, loss of Ca^+ caused by background collisions is also shown (grey points). Due to the constant DBB density n_{DBB} in the molecular beam, the reaction kinetics was modeled using a pseudo-first-order rate law, *i.e.*

$$\frac{\mathrm{d}}{\mathrm{d}t} n_{\mathrm{Ca^+}} = -\tilde{k}_{\mathrm{tot}} n_{\mathrm{Ca^+}}, \tag{3}$$

$$\frac{\mathrm{d}}{\mathrm{d}t} n_{\mathrm{C_4H_n^+}} = \tilde{k}^{(2)} n_{\mathrm{Ca^+}}. \tag{4}$$

Here, $\tilde{k}_{\mathrm{tot}} = \tilde{k}^{(1)} + \tilde{k}^{(2)}$, is the total decay rate of Ca^+ and $\tilde{k}^{(1,2)} = k^{(1,2)} n_{\mathrm{DBB}}$ are pseudo-first-order rate coefficients. The solutions are

$$n_{\mathrm{Ca^+}}(t) = n_{\mathrm{Ca^+}}(0)\,\mathrm{e}^{-\tilde{k}_{\mathrm{tot}} t}, \tag{5}$$

$$n_{\mathrm{C_4H_n^+}}(t) = n_{\mathrm{Ca^+}}(0)\frac{\tilde{k}^{(2)}}{\tilde{k}_{\mathrm{tot}}}\left(1 - \mathrm{e}^{-\tilde{k}_{\mathrm{tot}} t}\right), \tag{6}$$

where $n_{\mathrm{Ca^+}}(0)$ is the initial Ca^+ density at $t = 0$. Eqn (5) and (6) were independently fitted to the corresponding data (solid lines in Fig. 2b) to determine $\tilde{k}_{\mathrm{tot}}$. From the fit of eqn (6) to the $C_4H_n^+$ data, a value $\tilde{k}_{\mathrm{tot}} = 5.4(3) \times 10^{-3}\ \mathrm{s^{-1}}$ was found. Fitting the Ca^+ decay curve using eqn (5) yields a value of $\tilde{k}_{\mathrm{tot}} = 5.6(4) \times 10^{-3}\ \mathrm{s^{-1}}$ after background correction. The good agreement between the two independently determined values for $\tilde{k}_{\mathrm{tot}}$ confirms that $C_4H_n^+$ is indeed a product of the bimolecular reaction (2). The small yield of $C_4H_n^+$ indicates a small branching ratio $k^{(2)}/k_{\mathrm{tot}}$. The kinetic model then implies that $CaBr^+$ should be formed in much larger quantities, which is however not observed in the TOF-MS (Fig. 2a). An explanation could be increased loss of heavier product ions from the ion trap. The effective rf-trapping potential is inversely proportional to the ion mass, which leads to their localization further away from the laser-cooled Ca^+ core and renders sympathetic cooling less efficient.[33]

Conformer-specific rate coefficients

To investigate the effect of the molecular conformation of DBB on the reaction kinetics, the electrostatic deflector was used to prepare samples with well-defined conformational compositions. A density profile of the DBB molecular beam along the deflection coordinate (a deflection profile) was measured by vacuum ultraviolet (VUV) ionization of DBB at the position of the ion trap (Fig. 3a).[17] With the deflector turned off (deflector voltage 0 kV), the molecular beam contained a thermal 1 : 3.3 mixture of the *gauche* and *s-trans* conformers of DBB, respectively. At a deflector voltage of 13 kV, the *gauche*-DBB conformers were deflected away from *s-trans*-DBB in the beam and produced a shoulder at high deflection coordinates in the density profile. A Monte Carlo simulation of deflected DBB trajectories yielded good agreement with the experimental data for a rotational temperature of 1 K and independently

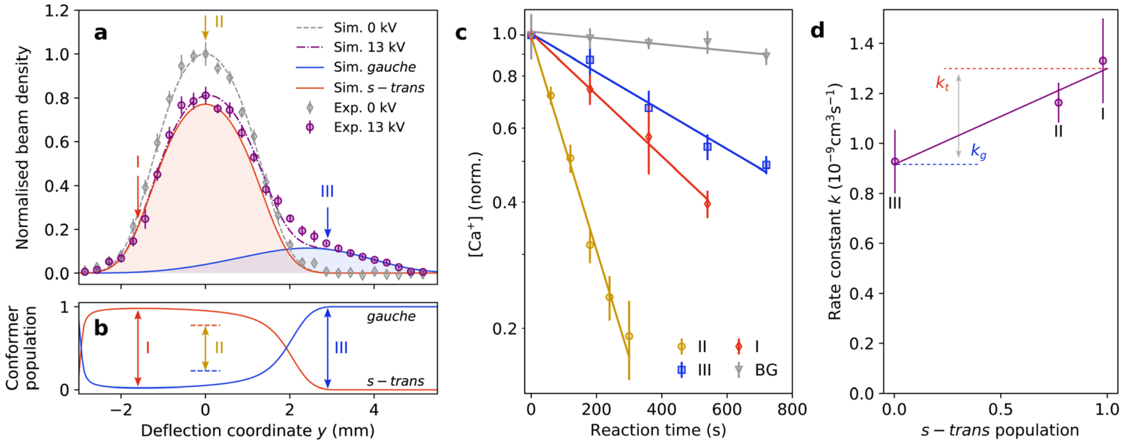

Fig. 3 Conformer-specific reaction rate coefficients. (a) Measurement of the DBB molecular beam density profile along the deflection coordinate for deflector voltages 0 kV and 13 kV. The data are in good agreement with Monte Carlo simulations which show the separation of the two conformers. (b) Conformer populations in the deflected molecular beam obtained from the Monte Carlo simulation. (c) Reaction kinetics measured in terms of the decrease of the Ca^+ ion number (normalized to its initial value) as a function of reaction time for the three positions I–III marked in (a and b) and a background measurement (BG). The exponential decay of the Ca^+ concentration implies pseudo-first-order kinetics. (d) Bimolecular rate coefficients extracted from the pseudo-first-order rate coefficient measurements as a function of the *s-trans*-conformer population with a linear fit (purple line). Error bars are standard deviations of three independent measurements.

measured beam velocity v_{beam} = 843(58) m s^{-1}.[17] At 13 kV, the time-averaged peak density of DBB was measured to be $n_{\text{DBB}} = 3.9(4) \times 10^6$ cm^{-3}.

The Monte Carlo simulation was used to determine the conformer populations as a function of deflection coordinate (Fig. 3b). Three beam positions, marked I–III in Fig. 3a and b, corresponding to the pure *s-trans* conformer (I), a thermal mixture (II) in the undeflected beam, and the pure *gauche* conformer (III), were chosen for reaction-rate measurements. In each position, the Ca^+ ion count was measured as a function of reaction time (Fig. 3c). The background loss rate of Ca^+ was determined separately by adjusting the molecular beam such that it did not hit the Coulomb crystal (grey data points in Fig. 3c). All traces exhibit an exponential decay of the number of Ca^+ ions which confirms the validity of using a pseudo-first-order rate law for the bimolecular reaction of DBB + Ca^+ with a constant DBB density. Pseudo first-order rate coefficients $\tilde{k}_{\text{tot},i}$ (i = I–III) were obtained by fitting exponential-decay models to the data and subtracting the corresponding background rate. From the $\tilde{k}_{\text{tot},i}$, the bimolecular rate coefficients $k_{\text{tot},i} = \tilde{k}_{\text{tot},i}/n_i$ were calculated using the DBB beam densities n_i at each position i = I–III in the deflection profile.

Fig. 3d shows the measured bimolecular rate coefficients k_i as a function of the *s-trans* population p_t obtained from the Monte–Carlo simulation. The bimolecular rate coefficient for the depletion of Ca^+ was modeled as the linear combination $k_{\text{tot},i} = p_{g,i}k_g + p_{t,i}k_t$ of the conformer-specific rate coefficients $k_{g/t}$ (*gauche*/*s-trans*). The weighting factors $p_{g/t,i}$ are the respective conformer populations at location i (Fig. 3b). A least-squares fit (solid line in Fig. 3d) with this model was applied to the data and yielded the bimolecular reaction rate coefficients $k_g = 0.92(11) \times 10^{-9}$ cm^3 s^{-1} for the *gauche*-conformer and $k_t = 1.30(13) \times 10^{-9}$ cm^3 s^{-1} for the *s-trans*-conformer. This implies a relative difference $r_{\text{exp}} = 2(k_g - k_t)/(k_g + k_t) = -0.35(7)$ by which the *s-trans*-conformer is observed to react faster than the *gauche*-conformer.

State-specific rate coefficients

Because the Ca^+ ions were constantly laser-cooled in the experiment, reactive collisions with DBB could occur in any of the electronic states (4s) $^2S_{1/2}$, (4p) $^2P_{1/2}$ and (3d) $^2D_{3/2}$ addressed by the laser excitation (see inset of Fig. 4a). Thus, the measured reaction rate coefficients represent an average over the states involved weighted by their populations. In order to obtain state-specific rate coefficients, reaction rates were measured in different configurations of Ca^+ state populations. Control over the populations was achieved by adjusting the frequency detuning Δ of the cooling and repumping lasers from the $^2S_{1/2} \rightarrow {}^2P_{1/2}$ (397 nm) and $^2D_{3/2} \rightarrow {}^2P_{1/2}$ (866 nm) transitions, respectively. The fluorescence of Ca^+ generated on the $^2S_{1/2} \rightarrow {}^2P_{1/2}$ transition was measured as a function of the laser detunings as well as polarization and modeled using optical Bloch equations to calibrate the average populations in the $^2S_{1/2}$, $^2P_{1/2}$ and $^2D_{3/2}$ electronic states (see ref. 34 and ESI,‡ Section S3). Fig. 4a shows the dependence of the level populations of Ca^+ on the detuning of the cooling laser, with the red circles representing the experimental $^2P_{1/2}$ state populations determined from the fluorescence measurements and the solid lines representing the results of the theoretical model. The excited-state $^2P_{1/2}$ and $^2D_{3/2}$ populations increase with decreasing detuning, while the ground-state $^2S_{1/2}$ population decreases.

To measure the reaction rate coefficients as a function of the excited-state population of Ca^+, a set of detunings Δ_{397} of the 397 nm laser labelled i–iii in Fig. 4a was chosen that samples a combined $^2P_{1/2}$ + $^2D_{3/2}$ population between 0.25 and 0.7. At each detuning, one rate measurement was conducted with pure *s-trans* DBB (molecular beam position I in Fig. 3a) and three measurements for pure *gauche* DBB

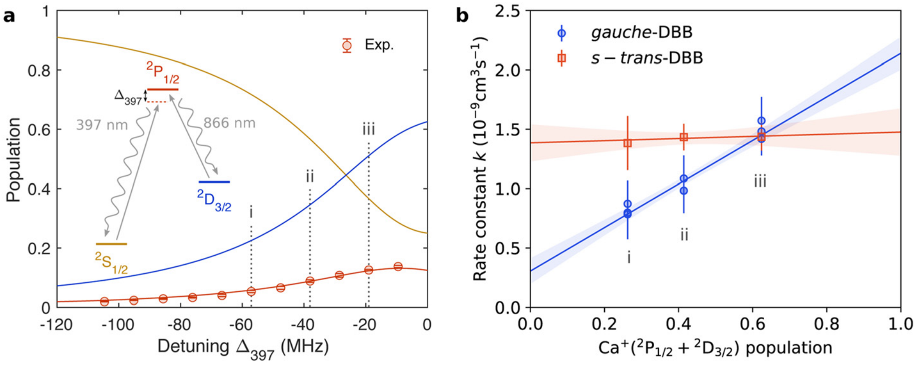

Fig. 4 Ca^+ state-dependent rate coefficients. (a) Dependence of the $^2S_{1/2}$, $^2P_{1/2}$ and $^2D_{3/2}$ state populations of Ca^+ on the detuning of the 397 nm cooling laser. Solid lines correspond to the theoretical model and data points represent the experimental $^2P_{1/2}$ state population determined from the ion fluorescence at 397 nm. The vertical lines labelled i–iii, denote the detunings at which rate measurements were performed. Inset: Energy-level diagram of Ca^+. (b) Results of the state- and conformer-resolved rate measurements at the detunings i–iii of (a). The lines are linear least-squares fits interpolating between bimolecular rate coefficients for Ca^+ in the ground (S) and excited states (P + D). Shaded areas correspond to a 90% confidence region. Error bars are fit errors of the individual rate measurements.

(molecular beam position III). Results of the state- and conformer-resolved rate measurements are presented in Fig. 4b. A linear model $k_{g/t,x} = (1 - p_x)k_{g/t;\mathrm{S}} + p_x k_{g/t;\mathrm{P+D}}$ was fitted to the measured rate coefficients $k_{g/t,x}$ as a function of the $^2P_{1/2}$ + $^2D_{3/2}$ excited state population p_x (x = i, ii, iii) to retrieve the ground-state ($k_{g/t;\mathrm{S}}$) and excited-state ($k_{g/t;\mathrm{P+D}}$) rate coefficients. Due to the strong correlation between the populations and rate coefficients in the $^2P_{1/2}$ and $^2D_{3/2}$ states obtained in the fit, no statements about their individual reaction rates could be made and only the effective rate coefficient averaged over both excited states is given.

Strikingly, the observed dependence of the rate coefficient on the Ca^+ excited state population differs strongly between the two conformers of DBB. While the rate coefficient remains nearly constant for *s-trans*-DBB, a clear increase with excited-state population is observed for the *gauche* conformer, pointing to a considerably reduced reaction rate for the *gauche* species with ground-state Ca^+. The fitted bimolecular rate coefficients of *s-trans* DBB with Ca^+ in ground and excited states, $k_{t;\mathrm{S}} = 1.4(3) \times 10^{-9}$ cm^3 s^{-1} and $k_{t;\mathrm{P+D}} = 1.5(4) \times 10^{-9}$ cm^3 s^{-1}, respectively, lie within one standard deviation from each other. For the *gauche* conformer, however, the fitted bimolecular rate coefficients are $k_{g;\mathrm{S}} = 0.3(2) \times 10^{-9}$ cm^3 s^{-1} for Ca^+ in its ground state and $k_{g;\mathrm{P+D}} = 2.2(3) \times 10^{-9}$ cm^3 s^{-1} for the excited states.

Adiabatic capture theory

Ion–molecule reactions often involve barrierless processes governed by long-range electrostatic interactions in which case capture models can be employed to model the kinetics.[21] In order to rationalize the different rate coefficients observed for the two DBB conformers in reactions with Ca^+, a rotationally adiabatic capture theory[20,30] was employed (see ESI,‡ Section S2). At the collision energy and rotational temperature of DBB in the present experiments, the calculation yields bimolecular rate coefficients of $k_{\mathrm{AC},g} = 2.4 \times 10^{-9}$ cm^3 s^{-1} for *gauche*-DBB and $k_{\mathrm{AC},t} = 1.3 \times 10^{-9}$ cm^3 s^{-1} for *s-trans*-DBB, with a calculated relative difference between the *gauche* and *s-trans* conformers of $r_{\mathrm{AC}} = 0.64$.

The measured rate coefficient for the *s-trans* conformer agrees with the calculated value within the uncertainty limits. By contrast, for the reaction of *gauche*-DBB with Ca^+ in its ground electronic state, adiabatic capture theory predicts a reaction rate coefficient about an order of magnitude larger than the experimental results. For reactions with electronically excited Ca^+ ions, however, capture theory and experiment again agree within the experimental uncertainties. It can thus be concluded that all but one combinations of both conformers of DBB and the electronic states of Ca^+ considered, the kinetics and dynamics of the title reaction can adequately be described by capture theory and are thus governed by long-range intermolecular forces, in this case ion–dipole interactions. The exception is the reaction of *gauche*-DBB with Ca^+ in its ground state, which was found to be considerably slower than the capture limit. Thus, in order to gain a more in-depth understanding of the reaction dynamics, additional computational studies were carried out including electronic structure calculations and reactive molecular dynamics simulations.

Potential energy surface and reaction pathways

To gain further insights into conformationally dependent reaction pathways of the title reaction and rationalize the experimental findings, quantum-chemical calculations of the PES were performed. Recent calculations at the explicitly correlated coupled cluster level of theory [CCSD(T)-F12] revealed that *gauche*-DBB lies 0.049 eV (2.22 kcal mol^{-1}) higher in energy than *s-trans* DBB and that an activation barrier of 0.18 eV (4.15 kcal mol^{-1}) is required to interconvert the two conformers by torsion along the central C–C bond.[17]

Fig. 5 depicts the energetically lowest reaction channels found by a scan of possible chemically distinct reaction pathways, as well as products, based on the assumption that the formation of the Ca–Br ionic bond is the driving force of the overall reaction. Fig. S6 of the ESI‡ shows all reaction pathways identified including ones with higher barriers. Intrinsic reaction coordinates (IRCs) and zero-point-energy corrections have been

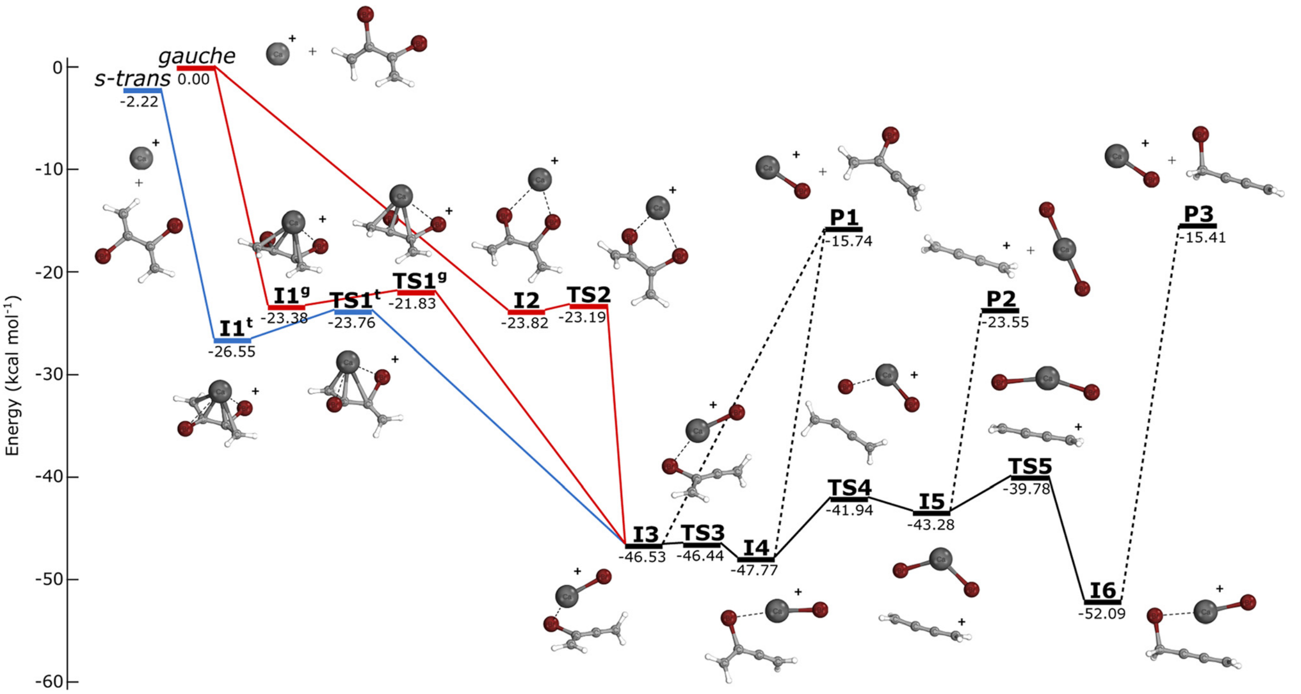

Fig. 5 Special points on the potential-energy surface for the reaction of *s-trans*- and *gauche*-DBB with ground-state Ca^+ calculated at the CCSD(T)-F12/VDZ-F12//B3LYP/def2-TZVPP level of theory (10 electron effective core potential for Br) including zero-point vibrational energy correction. Conformer-specific reaction channels are shown in red and blue, for *gauche*- and *s-trans*-DBB, respectively. Energies are given in kcal mol^{-1} with respect to the *gauche*-DBB + Ca^+ reactant. White, light grey, dark grey, and red spheres represent hydrogen, carbon, calcium, and bromine atoms, respectively. **I**, **TS**, **P** denote intermediates, transition states, and products.

obtained at the spin-unrestricted B3LYP/TZ level of theory. Electronic energies of the stationary points have been recomputed at the CCSD(T)-F12/DZ level of theory. All computational details, including quality checks for the IRCs and single-reference-character checks of the PES are described in the Methods section and the ESI.‡ Spin-restricted Hartree–Fock and B3LYP orbitals of the stationary-point structures were used for a chemical analysis of the reaction channels (the most important valence orbitals for every stationary-state geometry are depicted in Tables S4 and S5 of the ESI‡).

The reaction of Ca^+ (4s) $^2S_{1/2}$ with DBB can initiate *via* the addition of Ca^+ to either the bromine moieties or to the π-electron system of DBB. The relevant reaction intermediates are shown in Fig. 5 (**I2** and $\mathbf{I1}^{t/g}$). For both *s-trans*-DBB and *gauche*-DBB, an η^4-coordination of a singly occupied orbital of the π_4 system of DBB^- to Ca^{2+} emerges as a stable intermediate ($\mathbf{I1}^{t/g}$) with similar energies. In these intermediates, a single electron transfer from Ca^+ to DBB has occurred and the Ca^{2+} moiety is stabilized by strong σ-back-donation from the bromine atoms. Our results suggest that the *s-trans* adduct is energetically slightly favoured over the *gauche* adduct (energy difference ≈3 kcal mol^{-1} (0.13 eV)). For *gauche*-DBB, we also found an adduct intermediate **I2** similar in energy to $\mathbf{I1}^g$ in which both bromine groups coordinate to Ca^+. In this case, the calcium moiety has not undergone an electron transfer. These intermediates in the three entrance channels stabilize by 23–25 kcal mol^{-1} (1.00–1.08 eV) with respect to their reactant state *via* a barrier-less reaction path.

From all three entrance-channel intermediates ($\mathbf{I1}^{t/g}$ and **I2**), a Br^- migration from the DBB moiety to calcium over a low-lying transition state (activation energy <3 kcal mol^{-1} [0.13 eV]) was found forming intermediate **I3**. This intermediate displays a strong energetic stabilisation (≈46.5 kcal mol^{-1} [2.02 eV] with respect to the *gauche*-DBB reactant state) and exhibits an allene radical structure with the remaining DBB bromine coordinatively binding to $CaBr^+$. $CaBr^+$ dissociation from **I3** yields the product **P1** ($CaBr^+$, C_4H_4 Br) which is energetically stabilized by ≈15.7 kcal mol^{-1} (0.68 eV) with respect to the *gauche*-DBB reactant state. The ionic product of this pathway, $CaBr^+$, is observed in the experimental mass spectra (Fig. 2(a)).

Another pathway originating from **I3** *via* its conformer **I4** was found to feature a second Br^- migration to $CaBr^+$ *via* **TS4** to **I5**. In **I5**, perpendicular π_4 and π_2 systems have formed with the singly occupied molecular orbital (SOMO) being the HOMO of the π_4 system (for depictions of the orbitals see Table S4 of the ESI‡). Strong σ-back-donation from $CaBr_2$ stabilizes the uncommon electronic structure of the $C_4H_4^+$ species. Dissociation of $CaBr_2$ then results in the energetically most favoured product **P2** ($CaBr_2$, $C_4H_4^+$) where the SOMO exhibits a spiral π-system, typical for cumulenes. **P2** is energetically stabilized with respect to the *gauche*-DBB reactant state by ≈23.6 kcal mol^{-1} (1.02 eV). The ionic product of this pathway, $C_4H_4^+$, and fragmentation products thereof are observed in the experimental mass spectra (Fig. 2(a)). **I5** was also found to connect to a 1,2-migration of Br^- to the terminal carbon center, yielding **I6** which also exhibits an allene-radical electronic structure. This low-energy structure (stabilized by 52.1 kcal mol^{-1} (2.26 eV) with respect to the *gauche*-DBB reactant state) can then evolve *via* $CaBr^+$ dissociation to **P3** ($CaBr^+$, C_4H_4Br) which is close in energy to **P1**.

The initial conformer-specific reaction channels connect to the same intermediates after the first Br^- migration in the formation of **I3**. All barriers found are clearly submerged below the energies of the reactants, rendering all studied reaction pathways effectively barrierless. For the reaction of the *s-trans* conformer, this finding rationalizes the good agreement between the experimental and theoretical rate coefficient which was computed assuming barrierless capture dynamics. However, the barrierless minimum-energy paths displayed in Fig. 5 do not provide an explanation for the significantly lower reaction-rate coefficient observed for *gauche*-DBB.

Reaction rates from reactive molecular dynamics simulations

To gain further insight into the underlying reaction dynamics, reactive molecular dynamics simulations were performed on a full-dimensional machine learned PES trained on reference data at the DFT level using the PhysNet deep NN.[35] Reaction rates for both the *gauche* and *s-trans* conformers were computed from opacity functions derived from their respective reactive trajectories (see Methods).

Opacity functions for reactive collisions of the *gauche* and *s-trans* conformers are shown in Fig. 6. The results were obtained starting from 1000 initial conditions per impact parameter interval. To assess the role of rotational excitation in the dynamics, opacity functions were obtained for a range of rotational energies of the molecule corresponding to different rotational angular momentum quantum numbers *j*. The data suggest that the capture range for *gauche*-DBB is larger by ≈1 Å compared to the *s-trans* conformer irrespective of the molecular rotation. For both isomers, however, rotational excitation ($j > 0$) reduces the capture range leading to a smaller maximum impact parameter $b_{\max}$ and thus a reduced reaction rate. Note that $j = 20$ corresponds to rotational energies $E_{\text{rot}} \approx 0.09$ and 0.18 kcal mol^{-1} (3.90 and 7.81 meV) for *gauche*-DBB and *s-trans*-DBB, respectively, while for $j = 29$, the corresponding values are $E_{\text{rot}} \approx 0.19$ and 0.38 kcal mol^{-1} (8.24 and 16.48 meV). Under the present experimental conditions, both *gauche*- and *s-trans*-DBB populate considerably lower rotational levels with the largest population found in $j = 4$.[17] Thus, in the experiment $E_{\text{rot}} < 0.01$ kcal mol^{-1} (0.43 meV). Consequently, based on the present MD simulations, it can be surmised that the small rotational excitation of the molecules has a small influence on the observed reaction rates. We note, however, that these MD simulations, due to their purely classical-electrodynamics description, cannot reproduce effects due to weak-field-seeking behaviour in the approach of the molecule and ion (see Discussion below).

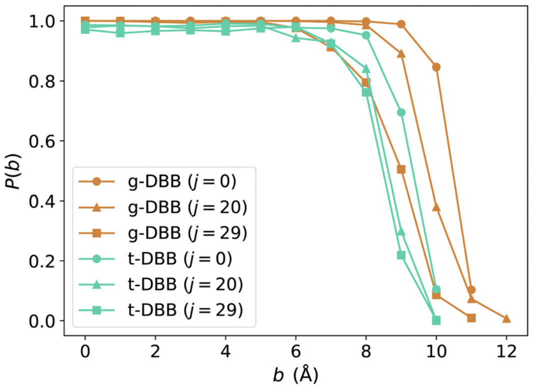

Fig. 6 Opacity functions for reactions of *gauche*- and *s-trans*-DBB with Ca^+ at a collision velocity v = 843 m s^{-1}. MD simulations were run for rotationally cold (j = 0) and excited (j = 20, 29) DBB to study the effect of rotation.

Table 1 Calculated rate coefficients for Ca^+ colliding with *gauche*-DBB and *s-trans*-DBB conformers at a collision velocity v = 843 m s^{-1}. Simulations were carried out with the PhysNet PES and used 1000 initial conditions for each interval of *b*. Units in cm^3 s^{-1}

	gauche	*s-trans*
PhysNet (j = 0)	2.5×10^{-9}	2.0×10^{-9}
PhysNet (j = 20)	2.2×10^{-9}	1.5×10^{-9}
PhysNet (j = 29)	1.7×10^{-9}	1.5×10^{-9}
Capture theory	2.4×10^{-9}	1.3×10^{-9}
Exp.	$3(2) \times 10^{-10}$	$1.4(3) \times 10^{-9}$

The reaction rate coefficients computed from the opacity function in Fig. 6 are listed in Table 1. Irrespective of rotation, the computed rate coefficients for *gauche*-DBB are larger by about 20% compared to the *s-trans* conformer. The rate coefficients obtained from the simulations are in good agreement with the capture theory and with experiment for the *s-trans* conformer, but fail to reproduce the experimental rate coefficient for reactions with *gauche*-DBB.

One difference between the two DBB isomers is that *gauche*-DBB features an ion–dipole barrier for certain directions of approach in the entrance channel. If the dynamics was sensitive to such a barrier in the entrance channel, this could explain the reduction of the rate for *gauche*- *vs.* *s-trans*-DBB. In order to test this hypothesis explicitly and to better characterize the underlying dynamics, 1000 trajectories with impact parameter $b = 0$ Å were analysed for both, *gauche*- and *s-trans*-DBB. For the polar *gauche* conformer, the long-range ion–dipole interaction with Ca^+ causes about 50% of the area of the molecule to be shielded by the repulsive ion–dipole barrier that rises up to ∼3 kcal mol^{-1} (0.13 eV). This might suggest that collisions along these directions lead to unproductive collisions and therefore reduce the total rate. For *trans*-DBB, lower repulsive barriers with heights <1 kcal mol^{-1} (0.043 eV) covering about ∼30% of the circumference were found along the approach of Ca^+ towards the two methylene groups.

The dynamics simulations, however, indicate that the ion–dipole barrier present for *gauche*-DBB does not reduce the reaction rate because during the collisions the reactants reorient towards the most favourable approach, *i.e.*, Ca^+ attacking the negative end of the molecular dipole, and thus avoid the barrier (Fig. 7). An alignment effect also occurs for *s-trans*-DBB as shown in Fig. 8. Because of these dynamics, it can be

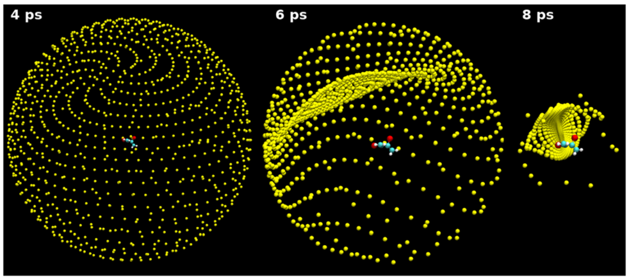

Fig. 7 Reorientation dynamics of the *gauche*-DBB + Ca^+ system over the course of reactive trajectories for impact parameter b = 0 Å. The figure shows the position of Ca^+ with respect to DBB 4, 6 and 8 ps after the start of the simulation for 1000 different initial conditions (collision angles). The orientation of DBB was fixed in the illustration. Intermolecular forces steer the Ca^+ ion towards the negative end of the molecular dipole, favouring the reaction pathway *via* intermediate **I2** in Fig. 5. The distances between the centre of mass of DBB and Ca^+ are ~41/25/7 Å after 4/6/8 ps. The full distributions of the distances is given in Fig. S9 of the ESI.‡

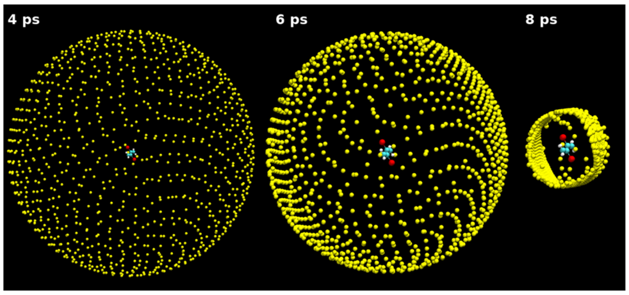

Fig. 8 Alignment dynamics of the *s-trans*-DBB + Ca^+ system over the course of reactive trajectories for impact parameter b = 0 Å. The figure shows the position of Ca^+ with respect to DBB 4, 6, and 8 ps after the start of the simulation for 1000 different initial conditions (collision angles). The molecular frame of DBB was fixed in the illustration. Intermolecular forces steer the Ca^+ ion toward a planar delocalization, or antialignment. After 8 ps, the system has transitioned toward a preferential reaction pathway passing through (the two symmetrically equivalent) $\mathbf{I1}^t$ states in Fig. 5. The full distributions of the distances of the collision partners are given in Fig. S10 of the ESI.‡

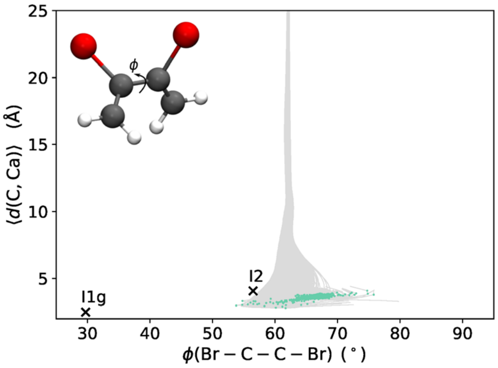

Fig. 9 Evaluation of the reaction pathway for the *gauche*-DBB simulations for impact parameter b = 0 Å and j = 0. Note that 62 out of the 1000 trajectories were excluded from the analysis, because they also transitioned towards *trans*-DBB before reaction. The analysis shows that the reaction happens exclusively *via* intermediate **I2** and does not sample the path *via* $\mathbf{I1}^g$ (see Fig. 5). The trajectories are shown up to reaction, *i.e.* up to the point for which a C–Br bond is broken and exceeds 3.0 Å (the equilibrium bond distance is 1.92 Å). The turquoise points mark the snapshot at which (one of the) Br–Ca ≤ 2.5 Å for the first time (the equilibrium distance of Br–Ca in **I3** is ~2.5 Å). The analysis of all 1000 trajectories is given in Fig. S12 of the ESI.‡

surmised that the barriers in the entrance channels of the collisions of both conformers do not play a significant role in the dynamics under the present conditions. As an additional verification that the barriers in the entrance channel are not responsible for the disagreement between observed and computed rates, additional simulations with collision energies decreased by up to a factor of ~3 were carried out. The result was an increase of the rate coefficient for the *gauche*-conformer in line with capture theory, which is, however, still at variance with the much smaller value obtained from experiment. Hence, the barriers in the entrance channel are not decisive for the differences in the reaction rates because the long-range intermolecular interactions orient *gauche*-DBB into a reaction-competent fashion and the barrier is never sampled for the collision energies relevant and considered here.

The most apparent difference between the two conformers is that *s-trans*-DBB only features one reaction pathway whereas for *gauche*-DBB, two paths are in principle accessible, see Fig. 5. However, a closer evaluation of the trajectories in Fig. 9 reveals that for the *gauche* species, the majority of reactive trajectories exclusively pass through intermediate **I2** in which the Ca^+ moiety is coordinated to the bromine atoms of DBB. While the small energetic differences between the two pathways are unlikely to account for this dynamic bias, this finding is in line with the reorientation dynamics discussed above: during the approach of Ca^+, the negative end of the molecular dipole formed by the bromine atoms of DBB orients towards the ion which directly leads to intermediate **I2** from where the reaction proceeds further, usually in a direct abstraction process. Conversely, for *s-trans*-DBB the reaction is found to proceed *via* two symmetric $\mathbf{I1}^t$ intermediates in which the Ca^+ ion is coordinated to the π electron system of the molecule as shown in Fig. S13 of the ESI.‡

Discussion

The current study presents a comprehensive experimental and theoretical characterisation of the state- and conformationally specific dynamics of the reaction of 2,3-DBB with Ca^+ ions. While excellent agreement between experiment and theory is obtained for the reactions of excited states of Ca^+ with both conformers of DBB as well as for ground-state Ca^+ with the *s-trans* species, the experimentally determined rates for ground-state Ca^+ colliding with *gauche*-DBB differ by almost an order of magnitude compared to those of the *s-trans* conformer, which is not reflected in the calculations. In search for explanations for this disagreement between experiment and theory, various analyses were carried out.

The lifetimes of the collision complexes were found to be generally short (<1 ps) for both DBB isomers. Thus, a possible slowdown of the reaction due to formation of a long-lived reaction intermediate cannot be the origin for the discrepancy between experiment and simulations for the *gauche* species. Typically, the simulations yielded direct abstraction reactions. Only for the minority of trajectories, lifetimes of the reaction complex longer than several vibrational periods (*i.e.*, longer than 1 ps) were observed. As discussed above, rotational excitation was found to change the reaction rates for both isomers in a similar fashion.

Concerning the quality of the PES, there are two main factors that influence the computed rates, first the quality of the PhysNet fit (*i.e.* how accurately the NN reproduces the *ab initio* reference data) and second, the chosen level of theory and basis set of the reference data.

First, the PhysNet representation of the global PES is accurate. Fig. S14 of the ESI‡ compares the *ab initio* with the PhysNet energies along two representative trajectories. The NN-based PES faithfully reproduces the DFT energies, which was also found when predicting energies for a test set that was not used during training. The out-of-sample mean absolute and root mean squared errors (MAE and RMSE) for predicting energies for $\sim$10 000 structures and covering an energy range of 230 kcal mol^{-1} (9.97 eV) amount to MAE(E) = 0.06 and RMSE(E) = 0.3 kcal mol^{-1} (2.6 and 13.0 meV), respectively. Thus, the quality of the fit can be judged excellent and fitting errors can be ruled out as a source of the discrepancy.

Second, an insufficient level of theory of the *ab initio* PES may be another reason for the discrepancy. A comparison between Fig. S6 of the ESI‡ and Fig. 5 illustrates the overall similarity of the B3LYP PES used for training the NN-PES and running the reactive MD simulations with the one obtained at the higher level of theory CCSD(T)-F12. However, as the energies of some stationary points differ by up to a few kcal mol^{-1}, an effect of the level of theory cannot be completely ruled out. For example, transition state **TS1**^{g} is higher in energy by 1.4 kcal mol^{-1} (0.06 eV) than **TS2** at the CCSD(T) level but in the B3LYP calculations, the ordering of the two states is reversed and the energy difference increases to 3.3 kcal mol^{-1} (0.14 eV). Notwithstanding the fact that the relevant barriers here are strongly submerged with respect to the energy of the reactants, we note that within transition state theory one order of magnitude difference in the rate corresponds to an energy scale of $\sim$1.5 kcal mol^{-1} (0.065 eV) which can, *e.g.*, be compared with an uncertainty of $\sim$4 kcal mol^{-1} (0.17 eV) in the ordering of **TS1**^{g} and **TS2** mentioned above.

In addition, the use of classical MD simulations as opposed to a full quantum treatment of the nuclear dynamics may be questioned. However, the masses of the atoms involved in the reaction as well as the energies along the reaction pathway are both large which make quantum effects as a source for the disagreement unlikely. Moreover, it was recently demonstrated that quasi-classical trajectory simulations yield energy-dependent rates that compare favourably with quantum wavepacket calculations for the C + O_2 → O + CO reaction in its electronic ground state down to collision energies of a few 10 K.[36]

On the other hand, molecules in low rotational states can display significant weak-field-seeking behaviour which leads to anti-orientation of the dipole in the electric field.[37] This effect is entirely quantum mechanical in nature and in the present case it is expected to be particularly important for intramolecular geometries between the long-range electrostatically dominated regime and chemical-bonding distances. From simple estimates and for the relevant ion–molecule distances of a few nanometer to a few 100 picometer, both the translation time and the re-orientation time of the molecular dipole in the field of the ion are on the order of some picoseconds. In the most obvious way, this would lead to ''inverted'' approach geometries and thus reduce the reaction rate for *gauche* DBB, but more generally this effect indicates that intricate details of the PES could be very relevant with respect to modified entrance-channel geometries and dynamics. In the present experiment, low rotational states for DBB are most prevalent and neglect of this in the MD simulations is potentially critical for correctly describing the reaction dynamics. Full dimensional quantum dynamics simulations for systems of this size are currently unfeasible, but a possible alternative is to precompute geometry-dependent Stark-effect-corrected effective interaction energies and add those to the energy function used in the MD simulations. This, however, is beyond the scope of the present work.

Lastly, multi-reference, non-adiabatic and spin–orbit effects could influence the dynamics in the present system. Checks for a possible spin contamination of the stationary points displayed in Fig. 5 remained inconspicuous, see Tables S2 and S3 of the ESI.‡ Thus, while these tests did not reveal any obvious multireference effects in the present system, a possible role of non-adiabatic dynamics cannot be ruled out until the lowest excited states of the system and potential crossings between them have been thoroughly explored which, however, is outside the scope of the present study. Along similar lines, the NN-based PES used in the trajectory calculations is unable to account for long-range charge transfer. All electronic effects are ''only'' included within the concept of a Born–Oppenheimer PES. It is conceivable that electronic structure calculations at almost all levels of theory are incapable of capturing such effects. As yet another possibility, it is also imaginable that spin–orbit interactions in the two conformers differ such as to stabilize a *gauche*-DBB intermediate to lower the rates.

Finally, we note that an isomeric effect was also observed in ref. 38 where the reaction of N^+ ions with *s-cis*-dichloroethylene ($C_2H_2Cl_2$) was found to be considerably slower than predicted by capture theory while the rate coefficient of the *s-trans* species agreed very well with the theoretical predictions. In that study, it was speculated that the reason for this discrepancy for *s-cis*-$C_2H_2Cl_2$ is a mismatch between the direction of most favoured attack for short-range charge transfer and the direction of the long-range approach of the collision partners along the axis of the molecular dipole. While this explanation is in line with the finding in the present system that the attack of Ca^+ occurs exclusively along the direction of the molecular dipole of the *gauche* conformer of DBB leading to the formation of intermediate **I2**, it does not rationalize the reduced reactivity in the present case according to our trajectory calculations.

Summary and conclusions

We performed reaction experiments with conformer-selected 2,3-dibromobutadiene from a molecular beam with trapped and laser-cooled Ca^+ ions. TOF mass spectra identified $C_4H_n^+$ and $CaBr^+$ as the main ionic reaction products. An analysis of the reaction-rate dependence on both the molecular conformation of DBB as well as the electronic-state population of Ca^+ revealed two kinetic regimes. With Ca^+ in either of the $^2P_{1/2}$, $^2D_{3/2}$ excited states, the kinetics were capture-limited for both DBB conformers and the rate coefficient of *gauche*-DBB was enhanced compared to the *s-trans* conformer due to the interaction of its permanent electric dipole moment with the ion. For reactions with Ca^+ in its $^2S_{1/2}$ ground state, the rate coefficient with *s-trans*-DBB was also found to be capture-limited. However, reactions of *gauche*-DBB were strongly suppressed to about one tenth of the capture limit.

The experimental findings were analysed using adiabatic-capture-theory calculations and reactive molecular dynamics simulations on a full-dimensional, machine-learned PES. For both isomers the abstraction reaction for forming $CaBr^+$ is direct with rare formation of an intermediate with lifetimes longer than 1 ps. For the *s-trans* conformer, the simulations yielded near-quantitative agreement with experiments for the rate coefficient. This is consistent with findings for reactive atom + diatom systems using similar computational approaches.[36] On the other hand, the computations overestimated the reaction rate for the *gauche* conformer, which features two possible reaction pathways, by an order of magnitude compared with experiment. Again, this has been found, for example, for the $MgO^+ + CH_4$ reaction, for which the computed rate differed from experiments by one order of magnitude but showing the correct temperature dependence.[39] The reason for the discrepancies in both cases may be limitations in the electronic structure methods that can be applied to the systems of interest given their size, omitting non-adiabatic effects, or neglect of purely quantum-mechanical re-orientation effects of the cold polar molecule in the electric field of the ion. Further studies are required to clarify these possibilities.

The present study highlights the important role of molecular conformation in gas-phase ion–molecule reactions already in moderately complex polyatomic systems. While previous studies of conformer-selected ion–molecule reactions[14,18] mainly uncovered conformational dependencies due to differences in long-range interactions, the current results suggest that short-range conformational effects strongly suppress the reactivity of the *gauche*-conformer, which still needs to be explained.

Moreover, although the actual – time-resolved – elementary dynamics of similarly controlled molecular systems were experimentally observed,[40] unravelling the underlying dynamics of bimolecular reactions such as the present one for now seems a formidable task, especially regarding problem of defining the starting time of the individual reactions but also the low occurrence statistics of ongoing reactions. The current combination of measuring time-averaged rates and molecular dynamics simulations consistent with experimental findings is a meaningful starting point for disentangling the chemical dynamics.

Methods

Molecular beam

The molecular beam was generated from DBB vapour at room temperature seeded in neon carrier gas at 5 bar. The gas mixture was expanded through a pulsed cantilever piezo valve (MassSpecpecD ACPV2, 150 μm nozzle diameter) with a repetition rate of 200 Hz. Before entering the reaction chamber, the molecular beam passed the electric deflector.[13,14] We measured a gas-pulse duration of 250 μs at the position of the center of the ion trap and a propagation velocity of the resulting molecular beam of $v_{\mathrm{beam}} = 843(58)\ \mathrm{m\ s^{-1}}$.[17]

Ion trap and TOF-MS

The radio frequency (RF) linear quadrupole ion trap was operated at a peak-to-peak RF voltage of $V_{\mathrm{RF,pp}} = 800$ V and a frequency of $\Omega_{\mathrm{RF}} = 2\pi \times 3.304$ MHz. Laser light at the frequencies of the cooling and repumping transitions of Ca^+ at 397 nm and 866 nm, respectively, was delivered by frequency-stabilized external-cavity diode lasers.[9] The Ca^+ fluorescence generated during the laser cooling was imaged onto a camera to obtain fluorescence images of the Coulomb crystals (see Fig. 1b).

The ion trap was radially coupled to a TOF-MS orthogonal to the molecular-beam propagation axis for the mass and quantitative analysis of reactant and product ions.[31] Two different modes of operation were used for the TOF-MS. For the determination of mass spectra of the reaction products, a low-resolution mode was used to extract ions into the TOF-MS by applying a 1 μs long pulse of 4.0 kV to the repeller electrode. For the rate measurements, additional high-voltage pulses, delayed by 0.45 μs, were applied to the extractor electrodes to selectively enhance the resolution for the Ca^+ and $C_4H_n^+$ species.[31] Ions were detected using a microchannel plate detector (MCP, Photonis USA) operated at a voltage of typically 2.3 kV placed at the end of the flight tube.

Ionization methods

Calcium atoms were ionized with femtosecond laser pulses from a Ti:Sapphire femtosecond laser (CPA 2110, Clark-MXR, Inc.) at a wavelength of 775 nm and pulse duration of 150 fs focused to a diameter of ≈30 μm at the center of the ion trap. A standardized procedure was used to ionize Ca atoms and ensure a constant size and composition of the ion Coulomb crystals as verified by TOF-MS. A pulsed vacuum-ultraviolet (VUV) light source at 118 nm, focused down to a spot size of roughly 100 μm, was used for soft ionization of the DBB molecules and to measure the deflection profiles.[17]

Quantum-chemical calculations

The PES presented in Fig. 5 was computed with spin-unrestricted Kohn–Sham density functional theory (UKS-DFT) using the B3LYP[41,42] and MPW1K[43] functionals with the def2-TZVPP[44] basis set and the Stuttgart effective core potential (ECP)[45] for the 10 inner shell electrons of bromine accounting for scalar-relativistic effects using the Gaussian09 software package.[46]

The functionals were chosen based on earlier studies for similar systems.[5,26,47] With both functionals, the same topology of intermediates, transition states, and intrinsic reaction coordinates (IRCs) was obtained. Minor differences between these methods are shown in an extended PES in Fig. S6 of the ESI.‡ Intrinsic reaction coordinates (IRCs) were found to connect all intermediates and transition states, barrierless reaction pathways connecting reactant and product states with the respective intermediates were found in all cases. Zero point vibrational energies were computed for all stationary points. Single point energies for all reaction paths were recomputed at the spin-unrestricted (for doublet states) or spin-restricted (for singlet states) CCSD(T)-F12b/VDZ-F12[48,49] level of theory using a spin-restricted HF/VDZ-F12 reference wave function with the Molpro program package.[50,51]

Intrinsic bond orbitals (IBOs)[52] of restricted open-shell B3LYP/def2TZVPP and HF/VDZ-F12 wave functions of the stationary point structures were computed for the chemical analysis. The orbitals depicted in Tables S4 and S5 of the ESI‡ have been visualized by the IboView program package.[53] The spin contamination of the wavefunctions for the stationary points were found to be low (see Tables S2 and S3 of the ESI‡).

Machine-learned PES and molecular dynamics simulations

Machine learning of the PES. A deep NN of the PhysNet type[35] was used to learn a full-dimensional representation of the PES for the collision reaction up to intermediates **I3**, **I4** and **I5** (see Fig. 5). PhysNet predicts energies, forces, dipole moments and partial charges of structures based on a descriptor that represents the local chemical environment of each atom.[35] Provided that PhysNet is trained on suitable *ab initio* data, it can be used for MD simulations with high accuracy instead of computationally much more expensive *ab initio* MD simulations at a given level of electronic structure theory.

Reference data including energies, forces and dipole moments was calculated at the B3LYP/def2-TZVPP using Orca.[54] Relevant geometries for the collisions of Ca^+ with both *gauche*- and *s-trans*-DBB were obtained by running Langevin dynamics using the semiempirical tight binding GFN2-xTB method.[55] Random momenta drawn from a Maxwell–Boltzmann distribution corresponding to 300 K were assigned to DBB (note that the resulting DBB configurations also contain configurations relevant to lower temperatures[56]). Diverse collision angles for the reaction were obtained by choosing the Ca^+ position randomly on a sphere around DBB before accelerating it towards DBB. After training PhysNet on this initial data set, new geometries were generated using adaptive sampling.[57,58] Adaptive sampling is used to detect regions on the PES which are underrepresented in the reference data set using an ensemble of PhysNet models. The final data set contained 191 982 structures covering the separated fragments and reaction products.

PhysNet was trained following the procedure outlined in ref. 35 and using the standard hyperparameters as suggested therein. The resulting PES of the studied system is given by

$$V = \sum_{i=1}^{N} E_i + k_e \sum_{i=1}^{N} \sum_{j>i}^{N} \frac{q_i q_j}{r_{ij}}. \tag{7}$$

Here, N and E_i correspond to the total number of atoms and the atomic energy contribution of atom i, k_e is Coulomb's constant, q_i is the partial charge of atom i and r_{ij} is the interatomic distance between atoms i and j. Note that the partial charges are corrected to guarantee charge conservation and the electrostatic energy is damped to avoid instabilities due to the singularity at $r_{ij} = 0$.[35]

Molecular dynamics simulations. Initial configurations for the reactive collision of DBB and Ca^+ were generated as follows: The center of mass (CoM) of DBB was placed at the origin of the coordinate system with space-fixed orientation and positions of Ca^+ generated by Fibonacci sampling[59] the unit sphere. Then, the separation between the CoM of DBB and Ca^+ was increased to 75 Å. Fibonacci sampling was used to generate evenly distributed points on the unit sphere, see Fig. S8 of the ESI.‡ A center-of-mass velocity of v = 843 m s^{-1}, consistent with experiment and corresponding to a collision energy of 2.86 kcal mol^{-1} (0.12 eV), was assigned to DBB whereas the Ca^+ cation was at rest. The impact parameter b was sampled uniformly in non-overlapping intervals (*i.e.* [0,1], [1,2], …, [14,15] Å) by displacing Ca^+ perpendicularly to the collision axis. 1000 trajectories were run per impact-parameter interval for b = 0 Å. The convergence of the opacity function (w.r.t. number of trajectories per impact parameter) was tested for *gauche*-DBB and impact parameters between b = 7 to 10 Å. Comparing the reaction probability obtained from 10 000 (denser Fibonacci lattice) and 1000 initial configurations yielded the same results within 1.5%.

Simulations were run in the *NVE* ensemble using the velocity Verlet integrator as implemented in the atomic simulation environment[60] with a time step of Δt = 0.25 fs. The simulations were terminated based on two distance criteria, *i.e.*, for r(C–Br) > 3 Å and r(Ca–Br) < 3 Å a reaction was considered to have occurred. Additionally, the simulations were stopped and considered "nonreactive" if, after initial approach, DBB and Ca^+ were separated by more than 30 Å without satisfying the criteria for a "reactive" trajectory. At the beginning of the simulation, the structure of DBB was optimized and remained vibrationally cold.

Two sets of simulations were carried out: The first was run without assigning any rotational energy to the DBB molecules. This is justified by the low temperature (few K) of DBB in the experiment. The second set included rotation of the DBB molecule to study the influence of classical rotation in general. For this, the moments of inertia I_A, I_B, I_C together with the three principal axes of rotation were determined and a rotation was assigned to the principal axis with lowest I_A. Simulations were carried out at different rotational energies $E_R = j(j+1)B$ where B is the rotational constant around the principal axis with lowest I_A.

Reaction rates. The opacity functions in Fig. 6 represent the fraction of reactive trajectories, *i.e.* $P = \frac{N_{\text{reac},b}}{N_{\text{tot},b}}$ at a given impact parameter b. Note that in Fig. 6 $b = 0$ corresponds to the simulations run with $b = 0$, while $b = 1$ corresponds to simulations run with $b = [0,1]$. The reactive cross section σ, from which the reaction rates were obtained, was calculated according to[61]

$$\sigma = 2\pi b_{\text{max}} \frac{1}{N_{\text{tot}}} \sum_{i=1}^{N_{\text{reac}}} b_i \quad (8)$$

where b_{max} is the largest impact parameter at which reactive events were observed, N_{tot} is the total number of trajectories, N_{reac} the number of reactive trajectories and b_i is the impact parameter of the reactive trajectory i. The reaction rate k is then determined from

$$k = \sigma \cdot v_{\text{rel}} \quad (9)$$

with $v_{\text{rel}} = 843\ \text{m s}^{-1}$ as in the experiments.

Data availability

The data that support the findings of this study are available on Github for the theory (**https://github.com/MMunibas/DBB_Ca**) and on Zonodo for the experiments (DOI: **10.5281/zenodo.7892235**).

Author contributions

A. K., J. W., and L. X. performed the experiments. A. K. analysed all data, with assistance from J. W., and performed the capture-theory calculations. L. X. simulated mass spectra with SIMION. P. S. and M. S. performed the quantum-chemical calculations. M. S. supervised the quantum chemical calculations. S. K. carried out and analysed reactive MD simulations. A. K., P. S., M. S., S. K., O. A. v. L., J. K., M. M., and S. W. wrote the manuscript. S. W., J. K., and M. M. conceived and supervised the project. All authors have read and approved the final manuscript.

Conflicts of interest

The authors declare no competing financial or non-financial interests.

Acknowledgements

We thank Philipp Knöpfel, Grischa Martin, Georg Holderied, and Anatoly Johnson at the University of Basel for technical support. We thank Ziv Meir for fruitful discussions. This work has been supported by the Swiss National Science Foundation under grants no. BSCGI0_157874 and IZCOZ0_189907, and the NCCR MUST, by Deutsches Elektronen-Synchrotron DESY, a member of the Helmholtz Association (HGF), and by the Cluster of Excellence "Advanced Imaging of Matter" (AIM, EXC 2056, ID 39 071 5994) of the Deutsche Forschungsgemeinschaft (DFG). O. A. v. L. has received funding from the European Research Council (ERC) under the European Unions Horizon 2020 research and innovation programme (grant agreement no. 772834). O. A. v. L. has received support as the Ed Clark Chair of Advanced Materials and as a Canada CIFAR AI Chair.

Notes and references

1 D. Smith and P. Spanel, *Mass Spectrom. Rev.*, 1995, **14**, 255–278.
2 P. Ehrenfreund and M. A. Sephton, *Faraday Discuss.*, 2006, **133**, 277–288.
3 M. Larsson, W. D. Geppert and G. Nyman, *Rep. Prog. Phys.*, 2012, **75**, 066901.
4 D. K. Böhme and H. Schwarz, *Angew. Chem., Int. Ed.*, 2005, **44**, 2336–2354.
5 J. Roithová and D. Schröder, *Chem. Rev.*, 2010, **110**, 1170–1211.
6 S. Willitsch, *Adv. Chem. Phys.*, 2017, **162**, 307–340.
7 J. Meyer and R. Wester, *Annu. Rev. Phys. Chem.*, 2017, **68**, 333–353.
8 D. Rösch, S. Willitsch, Y.-P. Chang and J. Küpper, *J. Chem. Phys.*, 2014, **140**, 124202.
9 S. Willitsch, *Int. Rev. Phys. Chem.*, 2012, **31**, 175–199.
10 B. Heazlewood and T. P. Softley, *Annu. Rev. Phys. Chem.*, 2015, **66**, 475–495.
11 F. Filsinger, U. Erlekam, G. von Helden, J. Küpper and G. Meijer, *Phys. Rev. Lett.*, 2008, **100**, 133003.
12 F. Filsinger, J. Küpper, G. Meijer, J. L. Hansen, J. Maurer, J. H. Nielsen, L. Holmegaard and H. Stapelfeldt, *Angew. Chem., Int. Ed.*, 2009, **48**, 6900–6902.
13 Y.-P. Chang, D. A. Horke, S. Trippel and J. Küpper, *Int. Rev. Phys. Chem.*, 2015, **34**, 557.
14 Y.-P. Chang, K. Dlugolecki, J. Küpper, D. Rösch, D. Wild and S. Willitsch, *Science*, 2013, **342**, 98–101.
15 T. Kierspel, D. A. Horke, Y.-P. Chang and J. Küpper, *Chem. Phys. Lett.*, 2014, **591**, 130–132.
16 D. A. Horke, Y.-P. Chang, K. Długołecki and J. Küpper, *Angew. Chem., Int. Ed.*, 2014, **53**, 11965–11968.
17 A. Kilaj, H. Gao, D. Tahchieva, R. Ramakrishnan, D. Bachmann, D. Gillingham, O. A. von Lilienfeld, J. Küpper and S. Willitsch, *Phys. Chem. Chem. Phys.*, 2020, **22**, 13431–13439.
18 A. Kilaj, J. Wang, P. Straňák, M. Schwilk, U. Rivero, L. Xu, O. A. V. Lilienfeld, J. Küpper and S. Willitsch, *Nat. Commun.*, 2021, **12**, 6047.
19 A. Kilaj, H. Gao, D. Rösch, U. Rivero, J. Küpper and S. Willitsch, *Nat. Commun.*, 2018, **9**, 2096.
20 D. Clary, *J. Chem. Soc., Faraday Trans. 2*, 1987, **83**, 139–148.
21 D. Clary, *Annu. Rev. Phys. Chem.*, 1990, **41**, 61–90.
22 A. Tsikritea, J. A. Diprose, T. P. Softley and B. R. Heazlewood, *J. Chem. Phys.*, 2022, **157**, 060901.
23 K. Mølhave and M. Drewsen, *Phys. Rev. A*, 2000, **62**, 011401.
24 P. F. Staanum, K. Højbjerre, R. Wester and M. Drewsen, *Phys. Rev. Lett.*, 2008, **100**, 243003.
25 S. Willitsch, M. T. Bell, A. D. Gingell, S. R. Procter and T. P. Softley, *Phys. Rev. Lett.*, 2008, **100**, 043203.
26 A. D. Gingell, M. T. Bell, J. M. Oldham, T. P. Softley and J. M. Harvey, *J. Chem. Phys.*, 2010, **133**, 194302.

27 F. H. J. Hall, M. Aymar, N. Bouloufa-Maafa, O. Dulieu and S. Willitsch, *Phys. Rev. Lett.*, 2011, **107**, 243202.
28 J. Greenberg, P. C. Schmid, M. Miller, J. F. Stanton and H. J. Lewandowski, *Phys. Rev. A*, 2018, **98**, 032702.
29 P. C. Schmid, M. I. Miller, J. Greenberg, T. L. Nguyen, J. F. Stanton and H. J. Lewandowski, *Mol. Phys.*, 2019, **117**, 3036–3042.
30 T. Stoecklin, D. C. Clary and A. Palma, *J. Chem. Soc., Faraday Trans.*, 1992, **88**, 901.
31 D. Rösch, H. Gao, A. Kilaj and S. Willitsch, *EPJ Tech. Instrum.*, 2016, **3**, 5.
32 W. Fang, L. Gong, Q. Zhang, X. Shan, F. Liu, Z. Wang and L. Sheng, *J. Chem. Phys.*, 2011, **134**, 174306.
33 B. Roth and S. Schiller, *Cold Molecules*, CRC Press, Boca Raton, 2009, p. 651.
34 H. Oberst, MSc Thesis, University of Innsbruck, 1999.
35 O. T. Unke and M. Meuwly, *J. Chem. Theory Comput.*, 2019, **15**, 3678–3693.
36 S. Goswami, J. C. S. V. Veliz, M. Upadhyay, R. J. Bemish and M. Meuwly, *Phys. Chem. Chem. Phys.*, 2022, **24**, 23309–23322.
37 Y.-P. Chang, F. Filsinger, B. Sartakov and J. Küpper, *Comp. Phys. Comm.*, 2014, **185**, 339–349.
38 C. Rebrion, J. B. Marquette, B. R. Rowe, C. Chakravarty, D. C. Clary, N. G. Adams and D. Smith, *J. Phys. Chem.*, 1988, **92**, 6572–6574.
39 B. C. Sweeny, H. Pan, A. Kassem, J. C. Sawyer, S. G. Ard, N. S. Shuman, A. A. Viggiano, S. Brickel, O. T. Unke, M. Upadhyay and M. Meuwly, *Phys. Chem. Chem. Phys.*, 2020, **22**, 8913–8923.
40 J. Onvlee, S. Trippel and J. Küpper, *Nat. Commun.*, 2022, **13**, 7462.
41 C. Lee, W. Yang and R. G. Parr, *Phys. Rev. B: Condens. Matter Mater. Phys.*, 1988, **37**, 785.
42 A. D. Becke, *J. Chem. Phys.*, 1993, **98**, 5648.
43 B. J. Lynch, P. L. Fast, M. Harris and D. G. Truhlar, *J. Phys. Chem. A*, 2000, **104**, 4811.
44 F. Weigend and R. Ahlrichs, *Phys. Chem. Chem. Phys.*, 2005, **7**, 3297.
45 A. Bergner, M. Dolg, W. Küchle, H. Stoll and H. Preuß, *Mol. Phys.*, 1993, **80**, 1431–1441.
46 M. J. Frisch, G. W. Trucks, H. B. Schlegel, G. E. Scuseria, M. A. Robb, J. R. Cheeseman, G. Scalmani, V. Barone, B. Mennucci, G. A. Petersson, H. Nakatsuji, M. Caricato, X. Li, H. P. Hratchian, A. F. Izmaylov, J. Bloino, G. Zheng, J. L. Sonnenberg, M. Hada, M. Ehara, K. Toyota, R. Fukuda, J. Hasegawa, M. Ishida, T. Nakajima, Y. Honda, O. Kitao, H. Nakai, T. Vreven, J. A. Montgomery, Jr., J. E. Peralta, F. Ogliaro, M. Bearpark, J. J. Heyd, E. Brothers, K. N. Kudin, V. N. Staroverov, R. Kobayashi, J. Normand, K. Raghavachari, A. Rendell, J. C. Burant, S. S. Iyengar, J. Tomasi, M. Cossi, N. Rega, J. M. Millam, M. Klene, J. E. Knox, J. B. Cross, V. Bakken, C. Adamo, J. Jaramillo, R. Gomperts, R. E. Stratmann, O. Yazyev, A. J. Austin, R. Cammi, C. Pomelli, J. W. Ochterski, R. L. Martin, K. Morokuma, V. G. Zakrzewski, G. A. Voth, P. Salvador, J. J. Dannenberg, S. Dapprich, A. D. Daniels, Ö. Farkas, J. B. Foresman, J. V. Ortiz, J. Cioslowski and D. J. Fox, *Gaussian 09 Revision D.01*, Gaussian Inc., Wallingford CT, 2009.
47 P. Redondo, A. Largo, V. M. Rayón, G. Molpeceres, J. Á. Sordo and C. Barrientos, *Phys. Chem. Chem. Phys.*, 2014, **16**, 16121–16136.
48 T. B. Adler, G. Knizia and H.-J. Werner, *J. Chem. Phys.*, 2007, **127**, 221106.
49 K. A. Peterson, T. B. Adler and H.-J. Werner, *J. Chem. Phys.*, 2008, **128**, 084102.
50 H.-J. Werner, P. J. Knowles, G. Knizia, F. R. Manby and M. Schütz, *Wiley Interdiscip. Rev.: Comput. Mol. Sci.*, 2012, **2**, 242–253.
51 H.-J. Werner, P. J. Knowles, G. Knizia, F. R. Manby and M. Schütz, *et al.*, *MOLPRO, version 2018.1, a package of ab initio programs*, 2018.
52 G. Knizia, *J. Chem. Theory Comput.*, 2013, **9**, 4834–4843.
53 G. Knizia, *Iboview Orbital visualization program (version 20150427)*, https://www.iboview.org.
54 F. Neese, F. Wennmohs, U. Becker and C. Riplinger, *J. Chem. Phys.*, 2020, **152**, 224108.
55 C. Bannwarth, S. Ehlert and S. Grimme, *J. Chem. Theory Comput.*, 2019, **15**, 1652–1671.
56 O. T. Unke, S. Chmiela, H. E. Sauceda, M. Gastegger, I. Poltavsky, K. T. Schütt, A. Tkatchenko and K.-R. Müller, *Chem. Rev.*, 2021, **121**, 10142–10186.
57 J. Behler, *J. Phys.: Condens. Matter*, 2014, **26**, 183001.
58 J. Behler, *Int. J. Quantum Chem.*, 2015, **115**, 1032–1050.
59 Á. González, *Math. Geosci.*, 2010, **42**, 49–64.
60 A. H. Larsen, J. J. Mortensen, J. Blomqvist, I. E. Castelli, R. Christensen, M. Dułak, J. Friis, M. N. Groves, B. Hammer and C. Hargus, *et al.*, *J. Phys. Condens. Matter*, 2017, **29**, 273002.
61 R. B. Bernstein, *Atom-molecule collision theory: a guide for the experimentalist*, Springer Science & Business Media, 2013.